A novel uncoupled quasi-3D Euler-Euler model to study the spiral jet mill micronization of pharmaceutical substances at process scale: model development and validation

Powder Technology 405 (2022) 117573

Contents lists available at ScienceDirect

Powder Technology

journal homepage: www.journals.elsevier.com/powder-technology

A novel uncoupled quasi-3D Euler-Euler model to study the spiral jet mill micronization of pharmaceutical substances at process scale: model development and validation

Carmine Sabia [a,b,*,1], Tommaso Casalini [a,1], Luca Cornolti [a], Marco Spaggiari [a], Giovanni Frigerio [c], Luca Martinoli [d], Alberto Martinoli [d], Antonio Buffo [b], Daniele L. Marchisio [b], Maurizio C. Barbato [a]

[a] Department of Innovative Technologies, SUPSI, Via la Santa 1 – Campus Est, 6962 Lugano, Switzerland
[b] Department of Science and Technology, Politecnico di Torino, Corso Duca degli Abruzzi 24, 10129 Torino, Italy
[c] Munit SA, Via Crocicchio Cortogna 6, 6900 Lugano, Switzerland
[d] Jetpharma SA, Via Sottobisio 42a/c, 6828 Balerna, Switzerland

HIGHLIGHTS

- A novel decoupled model is developed to study spiral jet milling at process-scales.
- The model exploits CFD simulations and 1D compartment-based calculations.
- Breakage parameters were defined availing of *ad hoc* micronization experiments.
- The proposed strategy works for brittle and semi-brittle substances.
- Model predictions are in good accordance with experiments.

GRAPHICAL ABSTRACT

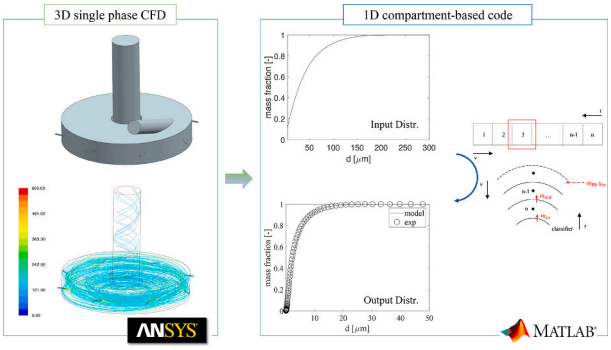

ARTICLE INFO

Keywords:
Spiral jet milling
CFD
Breakage kinetics
Particle size reduction
Process-scale micronization predictions

ABSTRACT

In this work we present a novel approach to model the micronization of pharmaceutical ingredients at process scales and times. 3D single-phase fluid-dynamics simulations are used to compute the gas velocity field within a spiral jet mill which are provided as input in a 1D compartmentalized model to calculate solid velocities along the radial direction. The particles size reduction is taken into account through a breakage kernel that is function of gas energy and local solid hold-up. Simulation results are validated against micronization experiments for lactose and paracetamol, comparing the model predictions with D10, D50 and D90 diameters values coming from Design of Experiments isosurfaces.

The developed model allows for a fair estimation of the outlet particle size distribution in a short computational time, with very good predictions especially for D90 values.

* Corresponding author at: Department of Innovative Technologies, SUPSI, Via la Santa 1 – Campus Est, 6962 Lugano, Switzerland.
E-mail address: carmine.sabia@supsi.ch (C. Sabia).
[1] These two authors equally contributed.

https://doi.org/10.1016/j.powtec.2022.117573
Received 30 December 2021; Received in revised form 27 April 2022; Accepted 25 May 2022
Available online 28 May 2022

1. Introduction

Spiral Jet Milling (SJM) is a widely used technique, employed to reduce the size of solid particles. It can be used for many purposes but its main application is the micronization of Active Pharmaceutical Ingredients (APIs) for the production of medicines.

A high-velocity gas flow (usually dry air or nitrogen), injected through a set of convergent nozzles within a micronization chamber, drives raw particles towards the spiral jet mill walls where high-energy particle-wall and particle-particle collisions take place, reducing their size progressively.

The swirled flow field established generates drag and centrifugal forces acting on the rotating particle along the spiral jet mill radial direction. The concurrent effect of the forces defines the size-dependent radial position of the particle, through an aerodynamic classification mechanism [1].

Gas pressure (p, bar(g)) and solid feed rate (FR, g/min) constitute the two parameters that can be changed to act on the spiral jet milling process and modify the output Particle Size Distribution (PSD) of powders.

SJM is particularly suitable to treat pharmaceutical products since it does not use any mechanical component to break down powders and there are no parts in relative motions one against the other. Because of this, there is no risk of powder contamination and the process does not deteriorate the active ingredients while the size reduction is taking place.

Micronization also carries some issues such as *caking*, which consists in the formation of large aggregates that rigidly stick on the walls of the spiral jet mill, reducing the useful volume and badly affecting the performance of the system by modifying the gas velocity fields and thus the classification, leading to undesired deviations of the final PSD and, therefore, to product out of target [1].

The physics behind the micronization process merges the complex fluid-dynamics of the gas inside the milling chamber with fluid-solid, solid-solid (aggregation and breakage) and solid-wall interactions (caking, where electrostatic and dispersion forces are involved), making the mechanistic modelling of the spiral jet milling a florid research field.

Nowadays, an established theoretical background still lacks, and the determination of the substance-specific operating condition is usually based upon expensive experimental campaigns driven by the technicians' experience.

Moreover, the detailed experimental characterization of the flow properties inside the apparatus is challenging or even not feasible, because sensors affect the swirling flow established within the grinding chamber and the probes may be damaged by collisions with high-velocity particles.

Due to this aspect, the development of numerical tools able to provide information at process level are very useful for SJM design optimization and for determining optimal process condition for new substances to obtain the target PSD.

In this context, computational fluid-dynamics (CFD) is usually coupled to a Discrete Element Method (DEM) solution to solve the particles dynamics in detail. This considerably simplifies SJM modelling but it remarkably increases the computational costs since CFD-DEM models need a transient solution for the trajectory of each discrete particle contained in the spiral jet mill. Assuming a holdup of 10 g and an average particle diameter of 20 μm [1] for a generic substance with density equal to 3000 kg m^{-3} (*e.g.,* lactose), the number of particles within the micronization chamber is of the order of 10^8–10^9. Moreover, depending on the level of coupling between phases, the model solution may need a very small time step, down to 10^{-9} or 10^{-10} s [2]. Hence, the required computational time is huge and this explains the lack of simulations at the characteristic time scales of the processes (minutes). In fact, to the best of authors' knowledge, works reported in scientific literature simulate only the first few instants of the spiral jet milling process.

A pioneering work of Han et al. [3] attempted to model the jet milling process by means of CFD-DEM simulations, including particles breakage and chipping through the implementation of the Ghadiri model [4–6]. Authors showed a good agreement between experimental and model results, stating that the solid feeding rate, nozzles angle and fluid pressure have a great effect on final PSD but they did not provide any information about the time step adopted and physical time simulated.

In a recent work, Bnà et al. [2] used CFD-DEM to study the motion of 1-way Lagrangian particles by simulating the first 70 ms of physical time. They deeply studied the gas velocity profiles and the classification mechanism in spiral jet mills. They tried to describe the influence that an increase of solid holdup has on collision energy and collision frequency, underlining how a soft-coupling between phases is not suitable to describe the interactions of gas and particles where the flow is heavily loaded (near outer walls of the micronization chamber).

Scott et al. studied the early stages of the micronization process (up to 100 ms of physical time) inside a spiral jet mill of 50 [mm] of diameter in order to understand the influence of holdup [7,9] and grinding pressure [8,9] on gas and particle flow patterns for a fully coupled (4-way) solution. It was shown that the gas velocity is influenced by the presence of particles in the periphery of the micronization chamber because of the fast shearing bed of solids that is formed near walls. The higher is the mass loading, the less is the velocity of the gas phase. Authors showed that this mechanism is important only near outer walls and they also underlined how an increase in grinding pressure augments the nozzles jet penetration, generating much more energetic particles collisions.

Bhonsale et al. [10] obtained the same results of Scott et al. [7–9] by simulating 150 ms of physical time for a system containing 100′000 particles. The collisions dynamics was studied with a temporal discretization of $2 \bullet 10^{-7}$ s.

These very recent works show that is currently not possible to simulate the entire micronization process, including particle-particle interactions and full mutual coupling between the gas and the solid phase at a process time scale.

This is due to the fact that the computational power offered by modern computers does not allow for a detailed simulation of spiral jet milling in reasonable times. Moreover, the complexity of the physics behind the micronization process makes the construction of robust and reliable particle-particle and particle-wall interaction models for aggregation, breakage and caking not trivial.

Few attempts have been made in the past and they are limited to the solution of the first 100–150 ms. of milling, allowing for the prediction of the very initial stages of the process. At these time scales, no useful information on the final fate of particles can be gathered. The large cost of many pharmaceutical compounds (up to hundreds of thousands of USD per kilo) still motivates the need of reducing experiments, pushing for the construction of reliable, robust and cheap computational tools able to model the whole process according to its characteristic time scale.

In this framework, the work presented hereafter aims at developing a novel quasi-3D modelling procedure, combining the single-phase velocity fields computed through a full 3D CFD simulation with a 1D compartmentalized model that solves the particles mass and momentum balances.

The particles size reduction mechanism is accounted for through a semi-empirical breakage kernel, tuned availing of specifically designed experiments where lactose and paracetamol powders were micronized. The predictions of the model are validated against results coming from response isosurfaces.

The here proposed modelling approach allows for the estimation of the outlet solid PSD at an affordable computational cost, usable to replace part of the expensive experiments currently used in the micronization industry.

2. Materials and methods

2.1. Materials

Lactose and paracetamol are chosen as representative process compounds because of their different breakage energy, large quantity of mechanical properties data available in literature and their low biological activity.

Moreover, they are cheap, usually available with short lead time and not dangerous.

Table 1 reports the hardness (H from nano-indentation), Young modulus (E) and yield pressure (p_Y) with related reference.

Lactose and paracetamol show a comparable hardness but they have a different elastic modulus; moreover, lactose has a higher ductility with respect to paracetamol, meaning that it can absorb more energy before rupture.

2.2. Design of experiment for micronization campaigns

The micronization campaigns are designed, performed and analyzed following an experimental approach based on the Design of Expert methodology (DoE); as a support, the Design-Expert 11 software (Design-Expert, Stat-Ease Inc., Minneapolis, USA) was employed.

Given the presence of a categorical factor (*i.e.,* powder typology), tests are split in two independent experimental plans, each consisting of the same number of runs in the same position of the design space.

Table 1
Paracetamol and lactose mechanical properties. # stands for the bibliography number in references.

Sub.	Ref.	#	H [GPa]	E [GPa]	p_Y [MPa]
Lactose	Masterson and Cao. Int. J. Pharm. 362 (2008) 163–171	[11]	0.51 ± 0.22 0.43 ± 0.08 0.18 ± 0.04	–	–
	Meier et al. Powder Technol. 188/3 (2009) 301–313	[12]	0.869	21.44	–
	Zuegner et al. Eur. J. Pharm. Biopharm. 62/2 (2006) 194–201	[13]	1.1	23.7	–
	O.M. de Vegt. PhD thesis U. of Groningen (2007)	[14]	0.288	9.7	103
	Wilson et al. Part II – cap. 9. ISBN: 978–1–119-28,549-6	[15]	–	–	165–178
Paracetamol	Cao et al. J. Pharm. Sci. 99/10 (2010) 4307–4316	[16]	1 ± 0.2	1.7 ± 0.1	–
	O.M. de Vegt. PhD thesis U. of Groningen (2007)	[14]	0.172	3.5	74.7
	Taylor et al. Powder Technol. 143–144 (2004) 179–185	[17]	0.42 ± 0.03	8.4	–
	Wilson et al. Part II – cap. 9. ISBN: 978–1–119-28,549-6	[15]	–	–	102–116

Two numerical continuous variables, *i.e.,* gas pressure (p) and powder feed rate (FR), are studied and their ranges are defined according to the process expertise and the already available results from previous studies.

A response surface – rotatable central composite design (CCD) [18], with 13 runs (described in Table 2) and capable of supporting a quadratic polynomial model, is built for both lactose and paracetamol powders. Five of the 13 runs are replicated to estimate the process variability and to get improved model precision in the center of the design space.

Responses, *i.e.,* the results of interest that are analyzed downstream of the experimental activities, are in both cases the sizes of the particles exiting the mill in terms of particle size distributions and D10, D50 and D90.

The capability of the models of finding statistically significant effects is assessed by means of the expected standard deviation (quantified at ±3 μm) and the acceptable uncertainty on the responses measurement (equal to ±5 μm).

2.3. Experimental set-up

Experiments were carried out availing of a spiral jet mill (called "MC" – see Fig. 1) served by 8 nozzles equally distributed and located around the central ring. Nozzles diameters and inclination angle are not reported for the sake of confidentiality.

The micronization equipment, as depicted by Fig. 1, was completed by the dosing unit twin-screw volumetric feeder K-Tron T35 and a cyclone dust separator with 600 mm top diameter, equipped with 16 sleeves antistatic polyester filter bag.

The linear relation between the solid mass-flow and the twin screw RPM has been verified by weighting the quantity of solid particles delivered by the system in 1 min of operation and checking 5 different velocities.

The feed-rate consistency, *i.e.* the dependency of the quantity of powder on the filling level of the dosing unit, has been studied by charging the hopper at 10%, 20%, 50% and 80% of its maximum capacity and running it at 310 g/ min. Each condition has been tested for 5 min of operation, checking the actual feed-rate at the beginning, in the middle and the end of the testing time.

Linearity results are shown by Table A.1. while measure consistency is described by values listed in Table A.2. in Appendix A.1.

Fig. 2 show that the dosing unit is able to provide a constant quantity of powder that increases linearly with the feeding screw speed (a) if the hopper filling level (F) is taken within 10% and 50% of the maximum value (b). The optimal value of F is therefore maintained for the whole process between 20% and 50%.

The PSD of raw and micronized powders was measured through a dry laser diffraction analysis with Sympatec HELOS BR with RODOS and

Table 2
Paracetamol and lactose DoE runs. p is the nozzles pressure while FR is the solid feed-rate.

	Paracetamol		Lactose	
Run	p [bar(g)]	FR [g/min]	p [bar(g)]	FR [g/min]
1	7	20	7	600
2	7	310	7	310
3	11	515	12	310
4	7	600	7	310
5	2	310	7	310
6	3	105	7	20
7	7	310	2	310
8	3	515	3	105
9	7	310	7	310
10	7	310	3	515
11	11	310	11	105
12	12	105	7	310
13	7	310	11	515

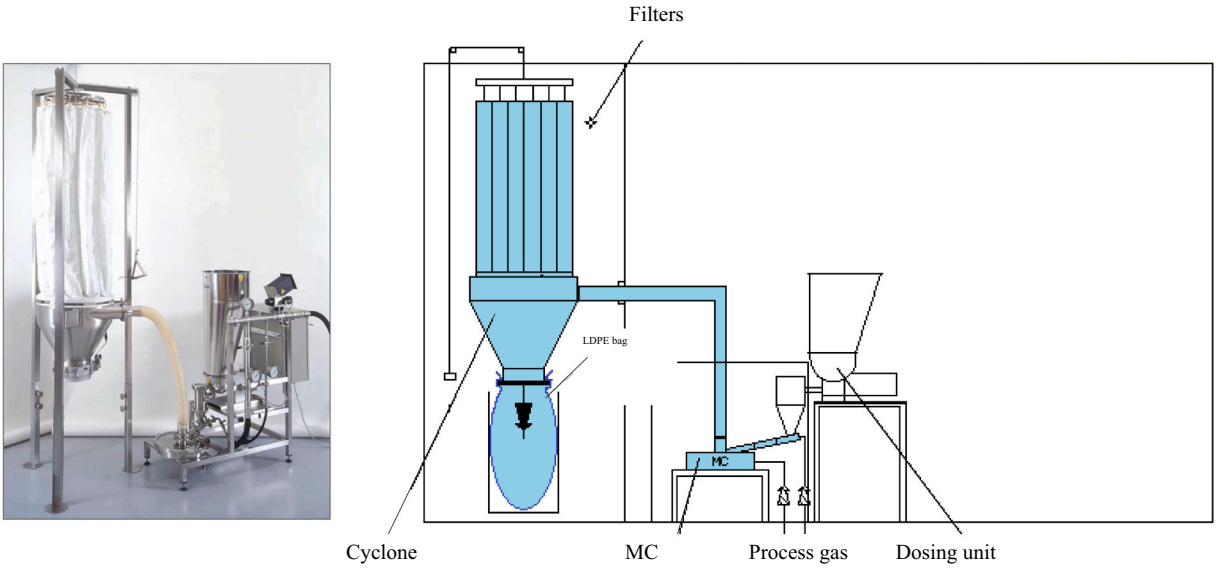

Fig. 1. Image of the micronization unit (left) and plant schematic with components disposition (right).

Aspiros configuration. Both lactose and paracetamol PSD method was validated according to *Eu.* Ph. <2.9.31 > .

The cumulative particle size distributions of the raw substances are visible in Fig. 3. Paracetamol (Sauter Mean Diameter – SMD equal to 41.36 μm) is provided with much larger size than Lactose (SMD equal to 11.25 μm).

Experimental D10, D50 and D90 of lactose and paracetamol are shown in Fig. 4. Micronization results show that paracetamol requires less energy to be broken with respect to lactose, consistently with literature data; indeed, paracetamol particle size is always smaller than lactose under the same process conditions.

This concept is better explained by computing the efficiency of the micronization process, calculated as:

$$r = \frac{D90_{exp,in} - D90^{i}_{exp,out}}{D90_{exp,in}} 100; \quad (1)$$

where the subscript exp refers to experimental, the subscript in is used for indicating the inlet (raw) powder size, the subscript out stands for the

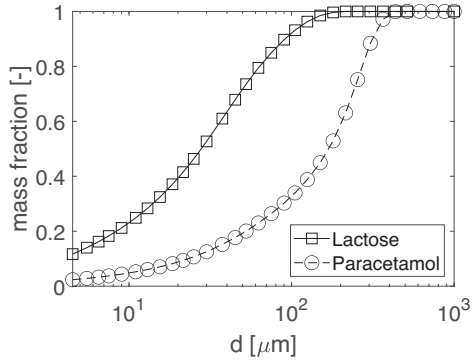

Fig. 3. Cumulative distributions of raw lactose and paracetamol used in micronization experiments.

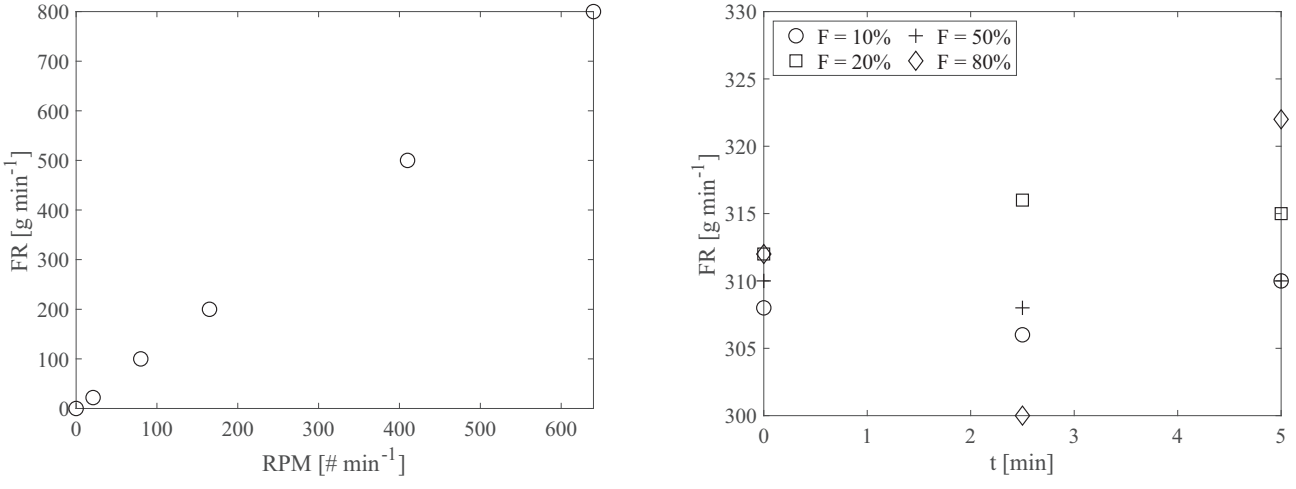

Fig. 2. Powder feed-rate - FR as function of dosing unit screw rotation velocity - RPM (a) and powder feed-rate - FR as function of sampling time- t (b). Filling level F is defined as the ratio between the actual mass of powder loaded in the hopper and the maximum quantity, $m_{s,max}$ = 25 kg.

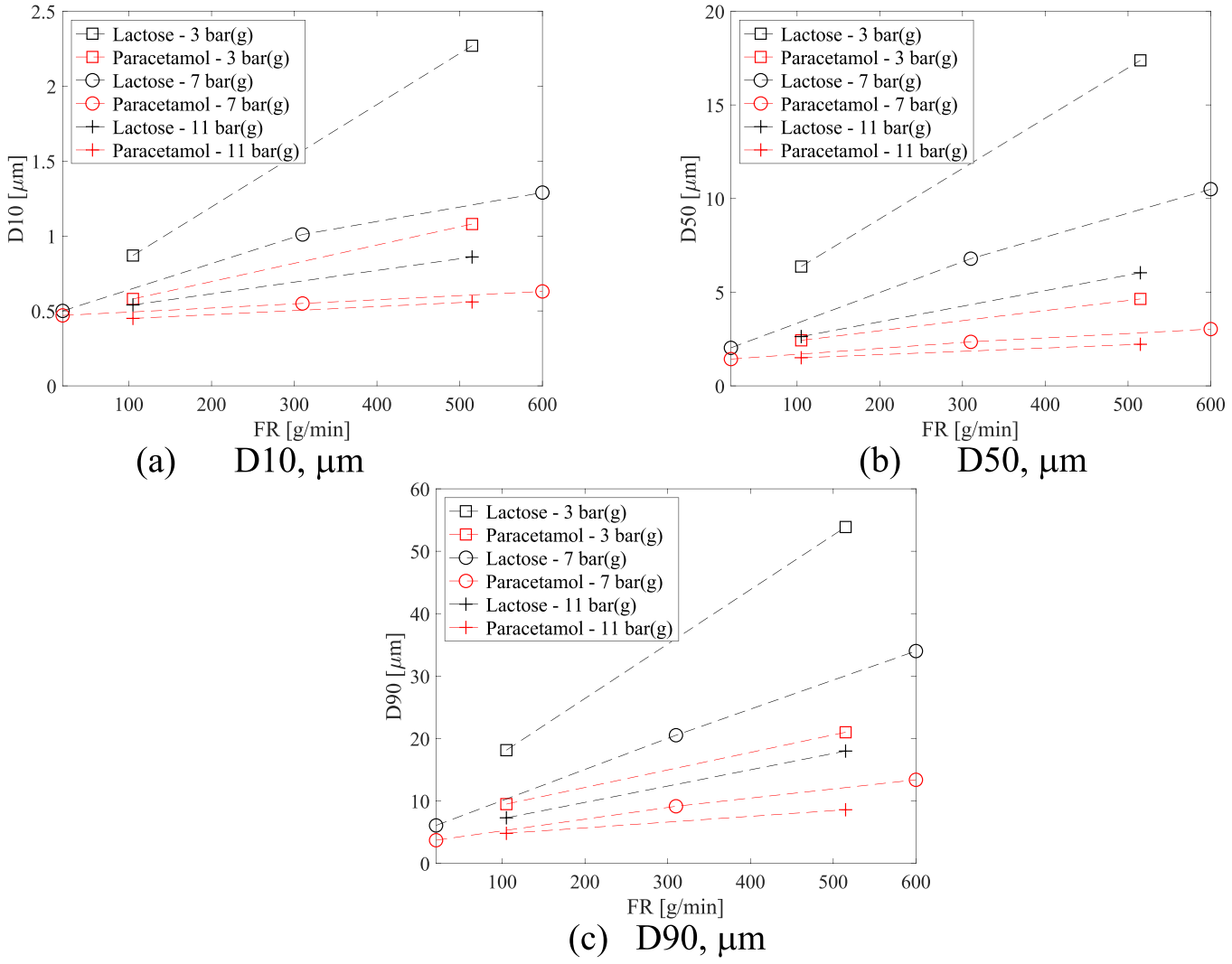

Fig. 4. Lactose and paracetamol micronization experiments.

outlet (micronized) size and the superscript i is used as experiment index.

Eq. (1) computes the percentage size reduction of the processed powder for D90. The latter is chosen for computing the micronization efficiency because it constitutes one of the most common particle size indicator for defining the process target in the powder processing industry As the relationship clearly shows, the r parameter is calculated taking the inlet D90 as reference and computing the relative size reduction for the two substances analyzed. An r equal to 0 corresponds to the raw powders while an r tends to 100% as the outlet D90 approaches to 0, stating that large r is obtained for particles undergoing to vigorous micronization.

Fig. 5 confirms that the size reduction is more efficient for paracetamol, due to its higher fragility. At high pressures, the percentage size reduction reaches 97.7% *circa* at medium feed-rates and 94.3% at high feed-rates for paracetamol while lactose is micronized with an efficiency of 92.0% and 80.3%, respectively.

As expected, at increasing the feed-rate FR corresponds an increase in average size while the higher is the nozzle pressure the lower is the particle average diameter.

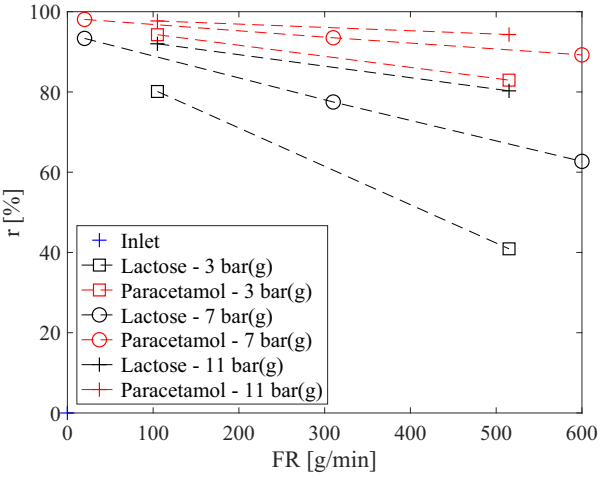

Fig. 5. Lactose and paracetamol micronization efficiency.

Data gathered through micronization experiments, in terms of mean size values as function of p and FR, will be used for tuning the breakage constants of the model and for validation purposes.

3. Model description

The comprehensive model follows the procedure detailed in the flow-chart of Fig. 6. The description of the sub-models of the various steps is provided in the following sub-sections. The first stage (green boxes) involves the computation of the gas velocity and density fields through the single-phase, steady-state, 3D CFD simulation of the SJM micronization chamber under given process conditions (in terms of pressure and temperature of the inlet gas pressure). In the second step, these data are lumped into 1D grid that evolved along the chamber radial direction to provide velocity fields to a compartmentalized model. Its formulaic description accounts for i) classification, by computing particles velocity through algebraic expressions and neglecting the influence of solids interactions on the gas flow field, assuming a one-way soft coupling between phases and ii) breakage, by solving mass balance along with a suitable kernel.

While it is known that particles tend to segregate near the walls of the micronization chamber (Scott et al. [6–9]), the gas-solid mixture can be assumed to be dilute (Sabia et al. [1]) in most of the SJM. This information justifies the previous assumption, at the base of this model.

Starting from radial-dependent gas velocity profiles as well as the inlet particle size distribution, the simplified 1D model solves the mass and momentum balance equations for each considered particle size and it provides the outlet PSD, which can be readily compared with its experimental counterpart if available. In more detail, substance-specific input parameters for breakage kernel were here estimated by fitting experimental outlet PSD through a multi-parameter regression availing of a genetic algorithm. The tuned model can be further employed to estimate the PSD for other process parameters. When a new compound is investigated, some experiments must be performed to provide the measured PSD of the processed powers to the 1D model to estimate the substance-specific parameters of the breakage kernel.

3.1. CFD model

This section provides a short description of the CFD model employed to estimate the velocity fields of the gas phase within the micronization chamber; more details can be found in Sabia et al. [1].

Sabia et al. also reports velocity, pressure, density and temperature contours, as well as the detailed analysis of the fluid cylindrical velocity components inside the micronization chamber for usual spiral jet mill process conditions.

The spiral jet mill fluid-dynamics is computed solving the Reynolds-Averaged Navier-Stokes (RANS) Equations discretized through a cell-centered Finite Volume Method (FVM). The single-phase flow fields of a compressible gas flow in an inertial reference frame with no gravity effects can be described by mass and momentum balances of the form (Batchelor [19]):

$$\frac{\partial \rho}{\partial t} + \nabla \bullet (\rho \mathbf{v}) = 0; \tag{2}$$

$$\frac{\partial (\rho \mathbf{v})}{\partial t} + \nabla \bullet (\rho \mathbf{v}\mathbf{v}) = -\nabla p + \nabla \bullet (\bar{\bar{\tau}}), \tag{3}$$

where $\bar{\bar{\tau}}$ is the stress tensor:

$$\bar{\bar{\tau}} = \mu \left[(\nabla \mathbf{v} + \nabla \mathbf{v}^T) - \frac{2}{3} (\nabla \bullet \mathbf{v}) \mathbf{I} \right], \tag{4}$$

with $\mathbf{v}$ equal to the 3D velocity vector, p is the pressure, μ is the molecular dynamic viscosity and $\mathbf{I}$ is the unity tensor.

An enthalpy equation, whose definition is given by Eq. (3.1) of Table 3, is used, together with the ideal gas law, to consider the gas compressibility effects and the energy variations related to it:

$$\frac{\partial \rho (h + \mathbf{v}^2/2)}{\partial t} + \nabla \bullet \left[\rho \mathbf{v} \bullet \left(h + \frac{\mathbf{v}^2}{2} \right) \right] = \frac{\partial p}{\partial t} + \nabla \bullet (\bar{\bar{\tau}} \bullet \mathbf{v}) + \nabla \bullet \left[\frac{(\lambda + \lambda_t)}{c_p} \bullet \nabla h \right]; \tag{5}$$

$$\rho = \frac{p}{RT}, \tag{6}$$

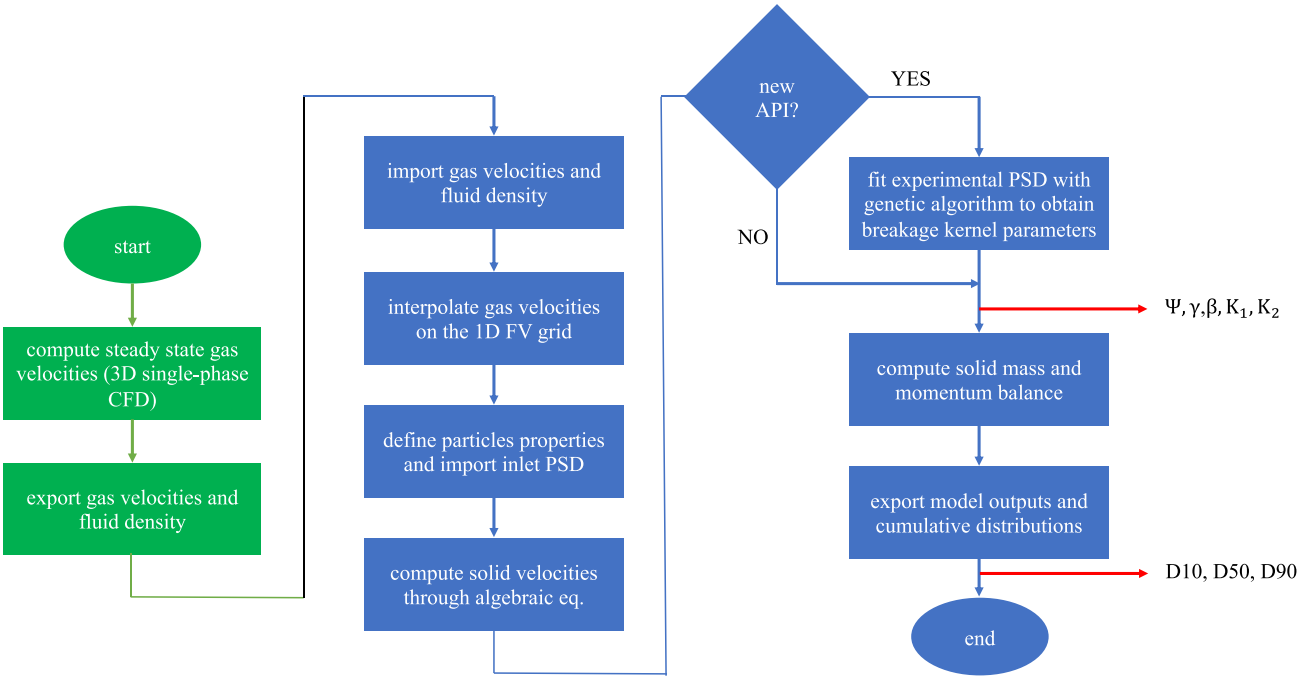

Fig. 6. Computational algorithm for coupling 3D single-phase CFD simulations (green boxes) with 1D compartmentalized solution for particle motion and breakage (blue boxes). (For interpretation of the references to colour in this figure legend, the reader is referred to the web version of this article.)

Table 3
Single-phase CFD model equations.

Equation	Nr.	Ref.
$h = e + \frac{p}{\rho} + \frac{v^2}{2}$	(3.1)	Vesteeg and Malalasekera [21]
$-\overline{\rho v_i' v_j'} = \mu_t\left(\frac{\partial v_i}{\partial x_j} + \frac{\partial v_j}{\partial x_i}\right) - \frac{2}{3}(\rho k \delta_{ij})$	(3.2)	Vesteeg and Malalasekera [21]
$v^+ = e^{\Gamma} v_{lam}^+ + e^{1/\Gamma} v_t^+$	(3.3)	Kader [22]
$Re_y \equiv \frac{\rho y \sqrt{k}}{\mu}$	(3.4)	Kader [22]
$\Gamma = -\frac{a(y^+)^4}{1 + by^+}$	(3.5)	Kader [22]

where h is the specific enthalpy, ρ is density, λ is the molecular thermal conductivity, λ_t is the turbulent thermal conductivity, R is the gas constant and T is the temperature.

The swirled nature and the extremely high velocity of the gas inside the micronization chamber generates a turbulent flow that is accounted for by solving the k − ε realizable model (Shih et al., [20]):

$$\frac{\partial(\rho k)}{\partial t} + \nabla \bullet (\rho k \mathbf{v}) = \nabla \bullet \left[\left(\mu + \frac{\mu_t}{\sigma_k}\right)\nabla k\right] + P_k + P_b - \rho\varepsilon - Y_M; \quad (7)$$

$$\frac{\partial(\rho \varepsilon)}{\partial t} + \nabla \bullet (\rho \varepsilon \mathbf{v}) = \nabla \bullet \left[\left(\mu + \frac{\mu_t}{\sigma_\varepsilon}\right)\nabla \varepsilon\right] + \rho C_1 S \varepsilon - \rho C_2 \frac{\varepsilon^2}{k + \sqrt{\nu\varepsilon}} + C_{1\varepsilon}\frac{\varepsilon}{k} C_{3\varepsilon} P_b, \quad (8)$$

where k is the turbulent kinetic energy, ε is the turbulent kinetic energy dissipation rate, μ_t is the turbulent viscosity, σ_k and σ_ε are the turbulent Prandtl number for k and ε respectively. P_k represents the generation of turbulent kinetic energy due to mean velocity gradients while P_b is the generation of k due to buoyancy. Y_M is due to fluctuating dilatations in ε while C_1, C_2, $C_{1\varepsilon}$ and $C_{3\varepsilon}$ are model constants.

Constitutive relations for Reynolds stresses derive from the eddy-viscosity concept and the Boussinesq approximation while relationships for near-wall modelling come from the two-layer concept. Equations and their bibliography sources are reported in Table 3.

Simulations are conducted through a real scale steady-state 3D CFD single-phase model built with Fluent by Ansys [23,24].

The flow is transonic or supersonic in many portions of the spiral jet mill domain (1.5 < Mach number < 2.5 in the region of space immediately downstream the nozzles outlet, just inside the micronization chamber, and 0.3 < Mach number < 0.8 in many other parts of the spiral jet mill) so a strong dependency of fluid density on pressure and temperature is expected. At such conditions, the evolving fluid (nitrogen) behaves like an ideal gas and the density is therefore computed availing of local temperature and pressure by means of the ideal gas law. Given the strong turbulent nature of the flow, the eddy viscosity is assumed to be largely predominant and the dynamic viscosity is kept constant to the nitrogen standard value.

The stability and robustness of the numerical solution is ensured by the Pressure-Based Coupled Solver of Fluent (PBCS), which calculates the pressure-correction and momentum equations in one step while the other are solved in a segregated manner.

Along with mass and momentum balances, the k − ε realizable model is solved to account for turbulence with a two-layer approach that switches from the actual computational of the velocity profile to wall-functions depending on the local y + value.

The Green-Gauss Node-Based method proposed by Barth and Jaspersen [25] is used to discretize gradients while pressure is interpolated at cell faces using the momentum equation coefficients as described by Rhie and Chow [26]. Momentum, enthalpy and turbulence transport equations are discretized with a second-order TFD scheme while the Pseudo-Transient Under-Relaxation concept proposed by Kelley and Keyes [27] is exploited to improve the convergence of the steady-state solution.

The investigated spiral jet mill computational domain is represented by Fig. 7. The simplified geometry maintains all the most important characteristics of the real system and the fluid volume simulated is composed by a cylindrical micronization chamber that hosts 8 nozzles. Nitrogen is fed by the nozzles and the powder feeder, while the only outlet consists in the central duct represented by Fig. 7.

The computational domain is discretized with ANSYS Meshing software, following a multi-block approach in order to build structured/paved computational grid with elements aligned to the flow direction along nozzles. This precaution allows for saving elements, maintaining a good description of flow properties where the most abrupt gradients are expected.

Fig. 8 shows the radially-evolving lines used to export cell-center radial velocity data and compute the velocity profile used in the Matlab code.

Five sampling lines lie on the ix-plane at different chamber heights to take into account the plates/wall presence in the upper and bottom part of the spiral jet mill (−1% and 1%), the expansion and the velocity peak induced by the nozzles (0%, same height of nozzles centerlines) and the "undisturbed" flow condition experienced in the center of the upper (−50%) and the lower (50%) chamber semi-half.

Data are exported as function of the radial position with full Cartesian coordinates and they are subsequently averaged to obtain a mean field usable in Matlab.

3.2. 1D compartmentalized model

The spiral jet mill micronization chamber is schematized as an isothermal reactor of cylindrical shape, discretized according to a cell-centered FVM. Based upon the SJMs working principle, the model assumes that the particles segregation takes place only along the radial direction. Axial inhomogeneities are neglected since the main mechanism governing both micronization and aerodynamic classification is related to the radial forces acting on particles [1].

The computational domain has been discretized into a series of well-mixed compartments of annular shape, each one representing a computational cell of the 1D domain (Fig. 9). All the properties are assumed homogeneous in every compartment. The particle size distribution is discretized into M classes selected within the range of the maximum size of the inlet PSD and the minimum particle diameter expected at the end of the micronization. The discretization scale is

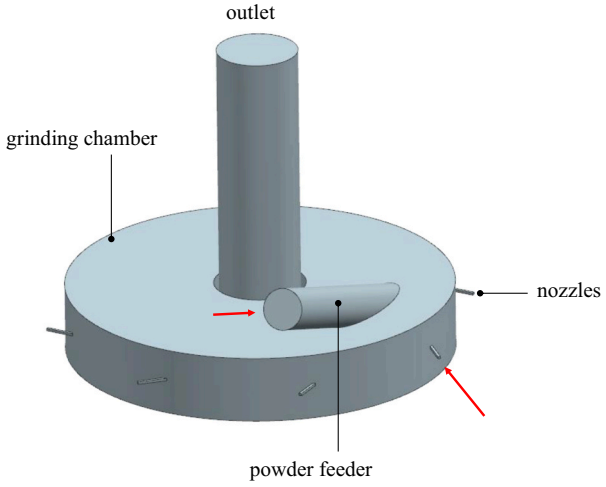

Fig. 7. Fluid volume of a simplified spiral jet mill. Red arrows mark the gas flow inlet regions (note that all the nozzles serve as gas inlet for the micronization chamber). (For interpretation of the references to colour in this figure legend, the reader is referred to the web version of this article.)

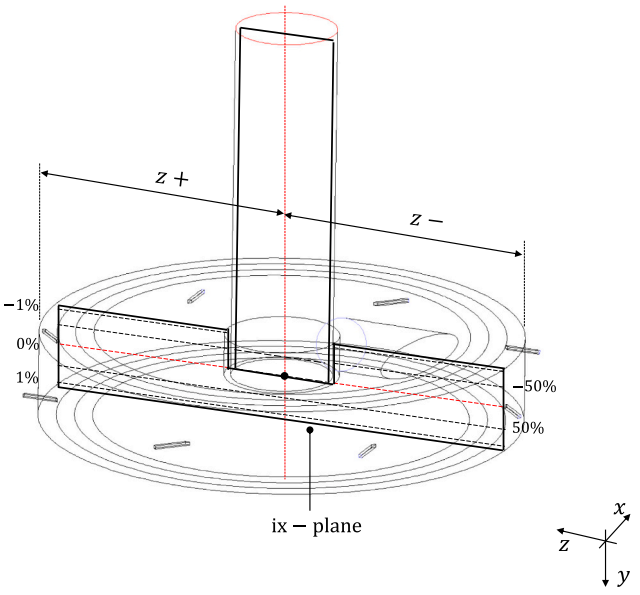

Fig. 8. Schematic of the inspection lines used to export velocity profiles.

logarithmic to increase the density of small size classes and to better describe the cumulative distribution.

Fig. 9 depicts a schematization of the computational domain, with the sign convention for radial velocity and the spatial coordinate (grid mapping).

According to the adopted assumptions, the mass balance for the generic *j*-th compartment and the *i*-th particle class has the form:

$$V_j\frac{d\omega_{ij}}{dt} = \dot{m}_{in,i} - \dot{m}_{out,i} + \dot{m}_{FR}x_{ij} + G_{ij}V_j = Av_{r,i}\omega_i\big|_{in} - Av_{r,i}\omega_i\big|_{out} + \dot{m}_{FR}x_i + G_{ij}V_j; \quad (9)$$

where ω_i, with units *kg* m^{-3}, is the mass concentration of particles with diameter d_i in the compartment *j*, V_j is the volume in m^3 of the *j*-th compartment, t is time, r is the radial coordinate, $\dot{m}_{in,i}$ and $\dot{m}_{out,i}$, with units kg s^{-1}, are the inlet mass flow from the adjacent compartments and their outlet mass flow to the adjacent compartments of particle class *i*, respectively. $v_{r,\,i}$ is the radial velocity of particles with diameter d_i, A is the face area corresponding to the lateral surface of a cylinder, $\dot{m}_{FR}$ is the mass feed rate, in kg s^{-1}, and G_i is birth or death rate of particles due to breakage defined in kg s^{-1} m^{-3}. In more detail, $\dot{m}_{FR}$ is equal to zero in every compartment except for the one that, according to the adopted radial grid, corresponds to the position of the feed in the experimental apparatus.

Variables ω_{ij} and x_{ij}, which is a weight function describing the relative mass fraction of each particle class passing through the inlet, are defined as MxN matrices where M is the total number of particle classes while N is the number of compartments.

Given that particle fragmentation is by far the predominant mechanism in driving the size reduction and particles dimensions at the outlet, aggregation events are not considered in this model at this stage.

Eq. (9) needs the evaluation of solid mass-flows at cell faces that can be computed by multiplying the solid radial velocities by the face mass concentration. The first quantity is computed by interpolating cell-centers velocities at compartments faces with a central difference scheme while the mass concentration is discretized implicitly with an upwind scheme.

The solid radial velocity as function of the particle diameter d_i and radial position (*i.e.,* for each compartment) is computed by solving the simplified steady-state momentum balance in which particles are allowed to exchange momentum with the fluid phase thanks to the drag force only:

$$\frac{\pi}{8}C_D\rho_p d_i^2\left(v_{r,j} - v_{r,ij}\right)\left|v_{r,j} - v_{r,ij}\right| - \frac{\pi}{6}\rho_p d_i^3\frac{v_{t,ij}^2}{r} = 0; \quad (10)$$

where C_D is the drag coefficient, ρ_p is the solid density, $v_{r,\,j}$ is the gas velocity in in the *j*-th compartment, $v_{r,\,ij}$ and $v_{t,\,ij}$ are radial and tangential velocities of the *i*-th particle class in the *j*-th compartment, respectively.

Eq. (10) constitutes a system of uncoupled non-linear relationships that is solved iteratively once the tangential velocity component of particles is known.

For the generic *i*-th particle class, the latter can be computed from the slip velocity equation developed by Konno and Saito [28] for pneumatic transport, already used in a recent work for describing the slip arising between the gas and the particulate phase in spiral jet mill modelling by Rodniaski et al. [29]:

$$v_{t,ij} = v_{t,j}\left(1 - 0.0638d_i^{0.3}\rho_p^{0.5}\right); \quad (11)$$

where $v_{t,\,j}$ is the local gas velocity in the *j*-th compartment computed through 3D single-phase CFD simulations.

The drag coefficient C_D and particles Reynolds number Re_p is computed according to the Schiller and Naumann [30] relationship:

$$C_D = max\left[0.44, \frac{24}{Re_p}\left(1 + 0.15\,Re_p^{0.687}\right)\right]; \quad (12)$$

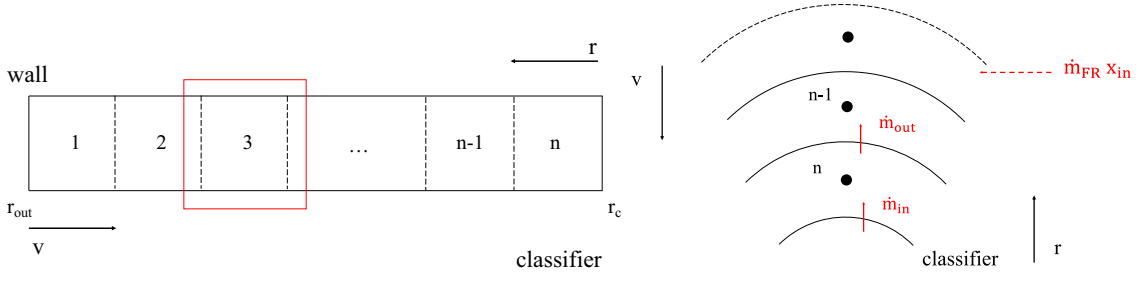

(a) computational grid schematic and radius-velocity sign convention

(b) graphical representation of mass fluxes entering and leaving a toroidal compartment of the model

Fig. 9. Spiral jet mill micronization chamber schematization: side view with 1D grid discretization (a) and top view with mass fluxes detail (b).

where:

$$Re_p = \frac{\rho_g |v_{r,j} - v_{r,ij}| d_i}{\mu_g}; \quad (13)$$

with ρ_g equal to the gas density and μ_g is the gas dynamic viscosity.

Writing Eq. (10) at steady-state implies the assumption that solid particles are accelerated instantaneously to the final velocity as result of the force balance acting on them. This hypothesis is valid for small particles immersed in a high velocity flow and it has been verified by solving the same momentum balance in transient state, using still particles as initial condition.

Simulations show that particles reach the steady-state motion in less than 10^{-2} s, a much shorter time the SJM process scales, corroborating the assumption.

This, together with the assumption of dilute flows conditions, allows for using steady-state velocities in the temporal integration of mass balances, significantly reducing the model complexity and the number of equations that must be solved.

The discretized form of Eq. (9) generates a system of NxM coupled linear first order ordinary differential equations. The coupling among equations is related to the implicit treatment of the convective fluxes, while the coupling among concentration of different particles sizes is achieved because of the source term G_{ij}, which is described in the following section. This system is solved with the ode15s solver provided by Matlab [31]. After about 5 s of physical time, the simulation reaches a steady state solution.

The model consistency is verified through the global mass balance that must be satisfied for each temporal time-step computed:

$$M_{in}(t) + M(t_0) = M(t) - M_{out}(t); \quad (14)$$

where $M_{in}(t)$ is the solid mass fed from time zero to time t, $M(t_0)$ and M (t) are the solid mass present in the domain at time zero (t_0) and time t respectively and $M_{out}(t)$ is the total solid mass escaped from the system from the beginning of the process until time t.

Terms of Eq. (14) can be computed as:

$$M_{in}(t) = \int_0^t \dot{m}_{FR} dt; \quad (15)$$

$$M(t) = \sum_{i=1}^{M} \sum_{j=1}^{N} \omega_{ij} \Delta V_j; \quad (16)$$

$$M_{out}(t) = \int_0^t \sum_{i=1}^{M} A v_{r,i} \omega_i |_{out,N} dt. \quad (17)$$

Eq. (14) can be used to derive an error function ε(t) that allows for evaluating i) the correct implementation of the model in a Matlab code and ii) the numerical inaccuracy introduced by the radial coordinate and particle diameter discretization:

$$\varepsilon(t) = \frac{M_{in}(t) + M(t_0) - M(t) - M_{out}(t)}{M(t)} 100. \quad (18)$$

Simulations show that the mass balance is always verified with ε(t) less than 1% for all the conditions tested.

3.3. Breakage kernel

Particles can break because of three different mechanisms: simple breakage, chipping and fragmentation (Salman et al. [32]). Pharma powders usually behave like brittle or semi-brittle material but their response is function of the particle diameter. Rowe and Roberts [33], indeed, showed that the breakage typology is dependent on a critical diameter that defines the deformation behavior, ranging from ductile for small particles ($d < d_{crit}$) to fragile for larger objects ($d > d_{crit}$).

The critical diameter is a strong function of the substance itself and its mechanical properties: elastic modulus, hardness and toughness play a major role in defining its value. Shariare et al. [34], for example, reported a critical diameter for Paracetamol of about 7 μm.

The description of such a behavior is taken into account through a semi-empirical model that weights the two different breakage dynamics by a parameter ψ while the dependency on particle size is considered through exponents γ and β.

Assuming a first-order breakage kinetics, the birth/death rate G_{ij} can be written availing of the concept of breakage function and selectivity firstly proposed by Kolmogorov and Epstein and later described by Austin [35] as:

$$G_{ij} = -S_{ij}\omega_{ij} + \sum_{k=1,}^{i} S_{kj}\omega_{kj} b_{ki}; \quad (19)$$

where S_{ij} is the selectivity associated to particles with diameter d_i in the *j*-th compartment. M is the total number of diameter classes, b_{ki} is the probability that the breakage of a particle of size *k* ends in a smaller particle *i*. Note that, with this notation, the ordering of the particle size is descending, that is, $d_1 = d_{max}$ and $d_M = d_{min}$.

The selectivity, computed according to Gommeren et al. [36,37], gives the fraction of particles selected for breakage and is computed as:

$$S_{ij} = \frac{K_1 M_j}{K_2 + M_j^{1.5}} p^2 \sqrt{\frac{d_i}{d_{max}}}; \quad (20)$$

where K_1, with units $g^{1.5}$ bar(g)$^{-1}$ s^{-1} and K_2, with units $g^{1.5}$, are substance-dependent parameters that have to be determined experimentally, M_j is the solid hold-up in the *j*-th compartment in g, p is the nozzle pressure in bar(g) and d_{max} is the largest possible diameter value that particles can assume with units μm.

The density breakage function b_{ki} is computed as [35]:

$$b_{ki} = B_{ki} - B_{k-1,i}; \quad (21)$$

where:

$$B_{ki} = \psi \left(\frac{d_k}{d_i}\right)^{\gamma} + (1-\psi)\left(\frac{d_k}{d_i}\right)^{\beta}, \text{for } \frac{d_k}{d_i} \leq 1. \quad (22)$$

Parameters ψ, γ, β of B_{ki} define the breakage mechanism and they have to be determined experimentally. Eq. (22) is valid only when $d_i \leq d_k$, *i.e.*, with the employed notation for $k \geq i$, otherwise $B_{ki} = 0$.

The semi-empirical nature of the model imposes a calibration based upon experiments for each tested substance. The Design of Experiments presented in Section 2 lists the operating conditions used for the experimental characterization performed with a MC spiral jet mill.

The model parameters are determined through a generalized version of the Differential Evolution (GDE3) genetic algorithm presented by Kukkonen and Lampinen [38] and later elaborated and implemented in Matlab by Baur [39].

4. Results

4.1. Model calibration

The usage of the genetic algorithm coupled to the compartmentalized model provides the lactose and paracetamol parameters shown in Table 4.

Results show that the importance of the first term in Eq. (22) (weight ψ) is limited for lactose while it is important for paracetamol. This confirms that the physical mechanism at the base of the particles fragmentation for the two substances is different, since lactose behaves, in general, like a ductile material while paracetamol tends to undergo to a fragile breakage.

Defining the relative error e% as the difference between experi-

Table 4
Model parameters for lactose and paracetamol.

Substance	ψ	γ	β	K_1	K_2
	[−]	[−]	[−]	[$g^{1.5}$ bar $(g)^{-1}$ s^{-1}]	[$g^{1.5}$]
Lactose	$6.97\bullet10^{-2}$	$5.00\bullet10^{-1}$	3.04	27.93	$1.48\bullet10^{-1}$
Paracetamol	$5.03\bullet10^{-1}$	52.70	$1.71\bullet10^{-1}$	40.36	$1.70\bullet10^{-1}$

mental and model data as described by Eq. (23), it is possible to evaluate the accuracy of the prediction obtained through the usage of parameters of Table 4.

$$e\% = \frac{|D_{i,exp} - D_{i,mod}|}{D_{i,exp}} 100. \quad (23)$$

Table 5 and Table 6 lists experimental (exp), model (mod) and relative error results for lactose and paracetamol at the same process conditions, respectively. The analysis is carried out on D10, D50 and D90 to evaluate the model performance on parameters describing the whole outlet distributions.

Table 5 shows that the best results are obtained for D50 and D90, with a maximum relative error of 28% *circa* in the first case and 20% in the second case.

Most of the constraints in terms of PSD of the final product are usually given on D90 and therefore the genetic algorithm is set to minimizes errors for diameters larger than D40. This motivates the worst prediction obtained for fines.

Table 6 shows that the model calibration for paracetamol is much stiffer than the lactose one, due to different breakage behavior whose particles with a wide distribution are subject to. Paracetamol raw powders, indeed, show a much higher Sauter mean diameter (41 μm) with respect to the one measured for lactose (11 μm) meaning that paracetamol particles undergo to a much vigorous size reduction process than lactose ones.

Large errors are encountered at low gas pressures while good predictions are obtained if high-energy density processes are simulated (high pressure and low/medium solid feed-rates).

Results show that the model does not fit properly data of wide inlet distributions. Eq. (20) show, indeed, that the selectivity formula is strongly dependent on the maximum particles size and, therefore, the shape of the function may change remarkably depending on the maximum particles diameter. Large errors are made especially for fines. This tendency is slightly mitigated if high-energy processes are treated (high pressure and low feed rate), coherently to the model assumption of having dilute flow condition.

The proposed kernel structure is not appropriate to model the fragmentation of particles population with wide distributions and a small critical diameter because the breakage may vary remarkably with the inlet size. Kernel parameters need, in this case, a pressure-dependent fitting to consider the behavioral change due to the different quantity of energy given to the micronization process.

Table 7 reports the pressure-dependent fitting of kernel parameters for paracetamol powders. Results clearly show that the paracetamol behavior at rupture notably change if the pressure is increased. Selectivity (Eq. (20)) and breakage probability (Eq. (22)) are computed at different pressures to show their dependency on particles dimensions and gas energy. Fig. 10, a. depicts selectivity as function of the particle diameter while Fig. 10, b. shows the breakage probability as function of particle diameter ratio (the ratio between the diameter of the particle *i* colliding against particle *k*). A remarkably different behavior is found between medium-pressure and high-pressure curves only for selectivity. The latter is higher at 7 bar(g) and it tends to increase if the particles diameter is augmented at any pressure. Curves obtained at 11 and 12 bar (g) are completely comparable, indicating that S_{ij} can be studied at two different pressure ranges only. Breakage probability, defined for $d_k/d_i \leq 1$, does not depend on pressure and the weighting parameter ψ is able to correctly model the different energy response of lactose and paracetamol. Exponent γ drives the shape of the breakage probability and model the different mechanism governing the fragmentation of paracetamol powders.

Fig. 10 clearly shows that only selectivity varies with pressure, meaning that parameters K_1 and K_2 of Eq. (20) need to be defined at each pressure level.

Fig. 11 depicts the fitting functions used to interpolate the pressure-dependent parameters defined in Table 8 through single-pressure model fitting.

As depicted, K_1 is a strong function of pressure and it decreases a lot as the energy of the flow increases. K_2 also shows a different behavior passing from medium to high-pressure ranges, doubling its value. A function of their ratio directly multiplies the grinding pressure in the selectivity formulation and they are, for this reason, important in defining the shape of S_{ij}. Both K_1 and K_2 clearly change value passing from medium- to high-pressure processes. This property is coherent with the selectivity shape showed by Fig. 10, a. β, instead, remains almost equal and the interpolant function returns a quasi-constant value, motivating the behavior of B_{ki}. The weighting function ψ assigns most of the breakage probability shape to the second term of Eq. (22), making negligible the large variations shown by γ.

This states that both the paracetamol and lactose fragmentation are driven by one breakage mechanism only with much of the physics complexity contained into the selectivity function formulation.

Fig. 12 shows the comparison between the output cumulative distribution function fitted from the model and data measured experimentally (exp) for a low pressure process (a., $p = 7$ bar(g) and FR = 20 g min^{-1}) and a high pressure process (b., $p = 11$ bar(g) and FR = 515 g min^{-1}) for paracetamol.

Results clearly show that the cumulative distributions are extremely well replicated if pressure dependent fitting is performed, especially at

Table 5
Comparison between the experimental (exp) and predicted model (mod) values for D10, D50 and D90 diameters of output PSD for lactose.

Case	D10			D50			D90		
	exp [μm]	mod [μm]	e [%]	exp [μm]	mod [μm]	e [%]	exp [μm]	mod [μm]	e [%]
7 bar(g) 20 g/min	0.59	0.64	9.54	3.85	3.97	3.08	11.86	12.99	9.54
7 bar(g) 310 g/min	1.14	1.60	39.68	7.75	9.88	27.51	23.13	27.76	19.99
7 bar(g) 600 g/min	1.33	2.04	53.00	10.50	12.99	23.70	34.33	33.31	2.99
11 bar(g) 105 g/min	0.55	0.41	26.20	2.68	2.37	11.44	7.29	8.23	12.92
11 bar(g) 515 g/min	0.90	0.95	9.54	6.08	5.89	2.99	18.14	17.60	2.99
12 bar(g) 310 g/min	0.98	0.62	36.60	5.06	3.74	26.20	13.80	11.86	14.09

Table 6
Comparison between the experimental (exp) and predicted (mod) values for D10, D50 and D90 diameters of output PSD for paracetamol.

Case	D10			D50			D90		
	exp [μm]	mod [μm]	e [%]	exp [μm]	mod [μm]	e [%]	exp [μm]	mod [μm]	e [%]
7 bar(g) 20 g/min	0.48	0.08	82.57	1.44	0.069	52.25	3.69	7.99	116.58
7 bar(g) 310 g/min	0.56	0.12	79.39	2.30	2.01	12.58	9.14	23.41	156.20
7 bar(g) 600 g/min	0.64	0.13	79.39	3.12	3.01	3.30	13.67	30.62	123.98
11 bar(g) 105 g/min	0.46	0.07	84.24	1.54	0.44	71.15	4.83	4.36	9.59
11 bar(g) 515 g/min	0.56	0.09	83.71	2.23	1.00	55.35	8.83	11.95	35.31
12 bar(g) 310 g/min	0.53	0.08	84.77	2.01	0.64	68.09	7.72	6.98	9.59

Table 7
Paracetamol breakage model calibration as function of grinding (nozzles) pressure @ 7 (FR = 20, 310, 600 g/min), 11 (FR = 105, 515 g/min) and 12 (310 g/min) bar(g).

Pressure	ψ	γ	β	K_1	K_2
[bar(g)]	[−]	[−]	[−]	$[g^{1.5}\ bar(g)^{-1}\ s^{-1}]$	$[g^{1.5}]$
7	$6.32\bullet10^{-2}$	21.04	2.02	160.04	$5.14\bullet10^{-1}$
11	$7.01\bullet10^{-2}$	2.49	2.10	83.56	1.27
12	$1.13\bullet10^{-3}$	$6.00\bullet10^{-1}$	1.91	61.27	$9.90\bullet10^{-1}$

high pressures.

Passing from single-pressure parameters set to the fitting functions depicted by Fig. 11, the error on D90 at 7 bar(g) and 20 g/min decreases from 117% *circa* to 35% while error on D90 at 11 bar(g) and 515 g/min decreases from 35% to 3% *circa*.

4.2. Model predictions

The results produced by the experimental campaign designed through the DoE for lactose and paracetamol described in Section 2. are used to build response equations for D10, D50 and D90.

The structure of the relationship describing the particles dimensions is given by Eq. (24), given in μm, and it is function of the gas grinding pressure (p – bar(g)), powders feeding rate (FR – g min^{-1}) and their interaction. The model needs a transformation through a new variable y′ that incorporates the original model output y:

$$y' = a + b \bullet p + c \bullet FR + d \bullet p^2 + e \bullet FR^2 + f \bullet p \bullet FR. \quad (24)$$

The coefficients and transformation variables are reported in Eq. (24) are listed in Table 8.

Due to the high quality of the response surfaces (adjusted R^2 always greater than 0.922), predictions obtained through Eq. (24) are considered as reference and they are used as "experimental data" to compare model values at process conditions different from those used for model calibrations.

Curves obtained through the DoE functions reported by Eq. (24) with the coefficients listed in Table 8 are marked in the following plots as "DoE".

The operating conditions tested to understand the model predictions capabilities are $p = 7$ bar(g), FR = 200, 350 and 500 g min^{-1} and $p = 11$ bar(g), FR = 200, 350 and 500 g min^{-1}; which are comprised within the validity ranges of the DoE used as reference.

Fig. 13 shows the comparison between predicted and experimental D50 and D90 values for lactose (a, b) and paracetamol (c, d) when the kernel parameters reported in Table 4 are used.

It is shown that an averaged-pressure set of the breakage kernel parameters properly predict the micronization behavior of lactose, especially at high pressure and medium/low feed rates. Predictions dramatically deteriorate for paracetamol, with errors of over than 180%, due to its different breakage behavior that is a strong function of pressure and particles diameter. Fig. 13, indeed, clearly shows that the

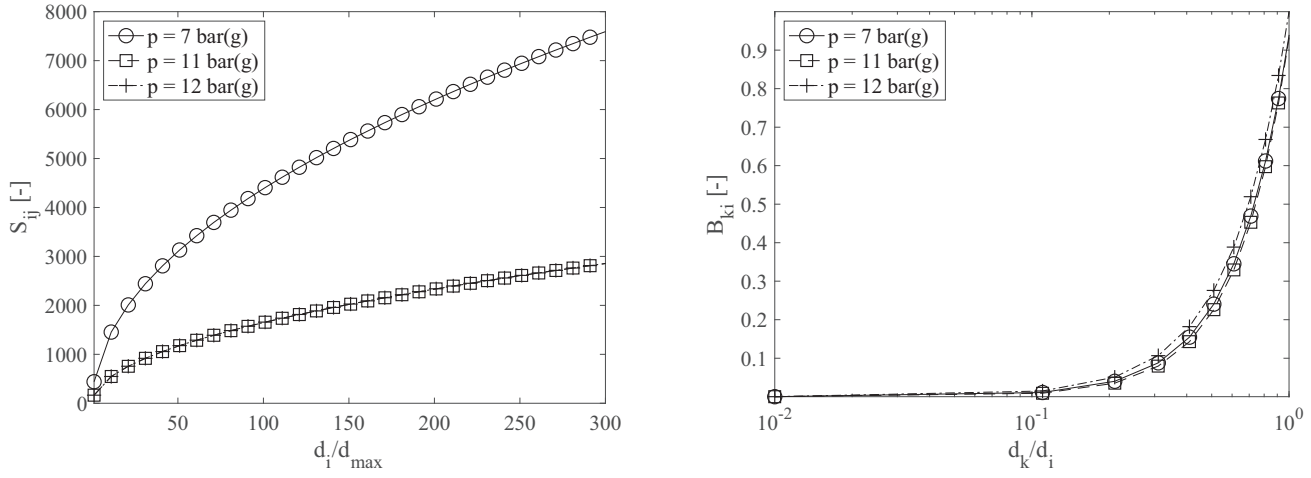

(a) selectivity (b) breakage probability

Fig. 10. Selectivity (S_{ij}) and breakage probability (B_{ki}) obtained from parameters optimization carried out at different pressures for paracetamol powders and assuming a 5 g hold-up.

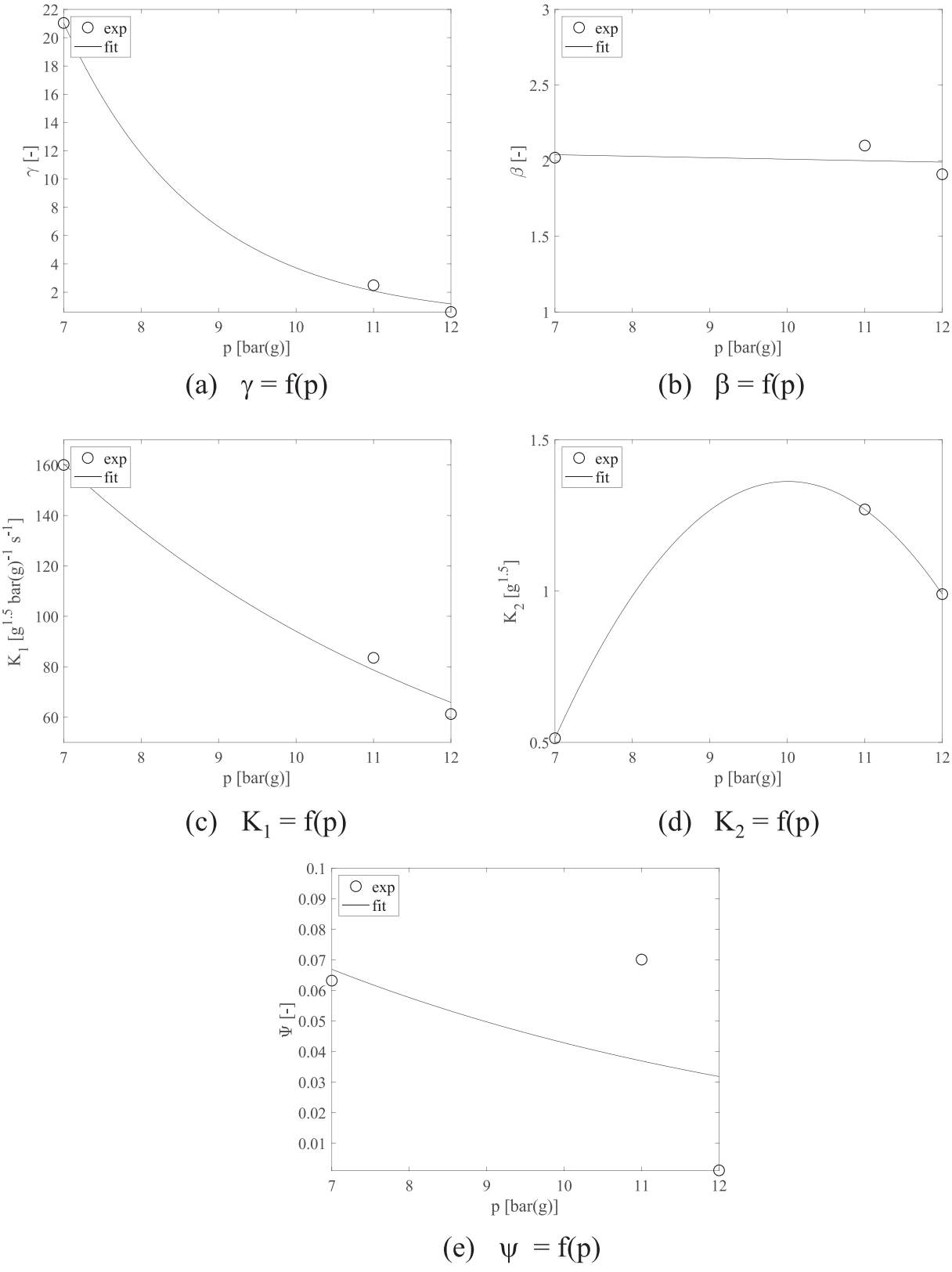

Fig. 11. Paracetamol breakage kernel parameters determined through pressure-dependent calibration (exp) and model fitting (fit).

Table 8
Reduced quadratic model equations parameters.

Substance	Variables		Coefficients					
	y	y'	a	b	c	d	e	f
Lactose	D10	y	1.5699	−0.3228	0.0044	0.0225	0	−0.0004
Lactose	D50	y	13.4393	−3.0161	0.0344	0.1864	0	−0.0026
Lactose	D90	$\log_{10}(y)$	1.4655	−0.1404	0.0024	0.0055	$-2.0395 \bullet 10^{-6}$	0
Paracetamol	D10	$y^{-2.38}$	0.5379	1.2844	−0.0093	−0.0606	$5.2914 \bullet 10^{-6}$	0
Paracetamol	D50	$\frac{1}{\sqrt{(y-0.5)}}$	0.5170	0.1138	−0.0013	−0.0053	$1.0526 \bullet 10^{-6}$	0
Paracetamol	D90	$\frac{1}{\sqrt{(y-0.5)}}$	0.2723	0.0591	−0.0010	−0.0028	$9.1840 \bullet 10^{-7}$	0

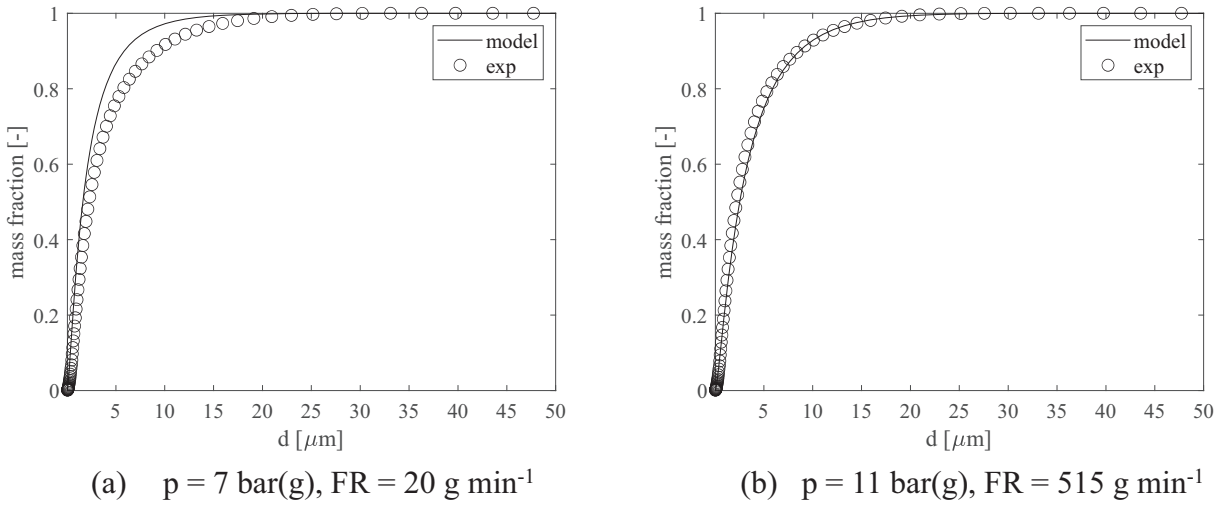

Fig. 12. Comparison between the cumulative distributions obtained through experiments (exp) and model fitting for paracetamol using fitting functions depicted by Fig. 11.

model well behaves in describing the micronization behavior at high pressure, *i.e.,* 11 bar(g), while it under predicts the particle size of particles when the process is conducted at medium specific energies. This is completely coherent to the important assumption done at the beginning of the decoupled model derivation of having dilute flow conditions, for which it is assumed that the solid volume fraction is not large enough to influence the motion of the carrier phase. This hypothesis is particularly true if the grinding pressure is high and the powder feed rate is low.

In order to improve the model prediction capabilities for cases with variable selectivity, a pressure-dependent tuning is performed and a parameters definition based upon the flow energy content is implemented.

Fig. 14 gathers results obtained availing of constant kernel parameters (black markers) and results computed though the usage of parameters functions shown by Fig. 11 (red markers). Notice that vector x stores the kernel parameters such that x = const refers to the constant kernel parameters set while x = f(p) is the notation used for the pressure-dependent parameters set.

Results show that pressure-dependent parameters drastically improve the prediction capabilities of the model even when a substance with a complex breakage mechanism is considered. Relative errors, computed according to Eq. (24), are in average comprised between 7% and 15% but always lower than 22.6% (worst case obtained for D90 prediction at 7 bar(g) and 350 g min^{-1}).

If compared to fully coupled CFD-DEM simulations, the presented model framework provides process-scale results in a tremendously shorter computational time.

Once the kernel parameters for an API are determined, the model calculates the final output PSD in approximately 5 min of computational time through a serial process on a 4-core computer with 16 GB RAM.

5. Conclusions

A novel uncoupled quasi-3D Euler-Euler model has been built to study the spiral jet milling at process scales.

The proposed computational procedure calculates the 3D single-phase CFD gas velocity fields and use them in a 1D, radially evolving compartmentalized model to compute particles mass and momentum balances. The solid phase is advected availing of an algebraic velocity formulation and the breakage kinetics is computed according to a semi-empirical model tuned over experimental data.

Ductile (lactose) and fragile (paracetamol) substances are analyzed.

In accordance with the model assumption of dilute flow conditions, the best agreement between the model and the experimental results is obtained for highly energetic processes.

Results show that the computational model developed well predicts the output PSD of ductile particles with a single-set of breakage kernel parameters, containing errors within 50%. Fragile powders, which exhibit a variable selectivity depending on pressure and particles diameter, need a pressure-dependent fitting for breakage parameters and predictions show very good agreement to experiments, with a maximum error of 22.6% obtained for D90 at 7 bar(g) and 350 g min^{-1}.

The developed computational procedure is very fast if compared to fully coupled Eulerian-Eulerian or Eulerian-Lagrangian simulations and it provides reliable results at process scales (steady-state micronization for real apparatus) with few minutes of calculation times with good accuracy.

The model predictions quality deteriorates as the pressure range is enlarged, especially for raw powders with wide inlet distributions. In these cases, a pressure-dependent kernel parameters tuning is needed to include all the mechanisms that drives particles size reduction and

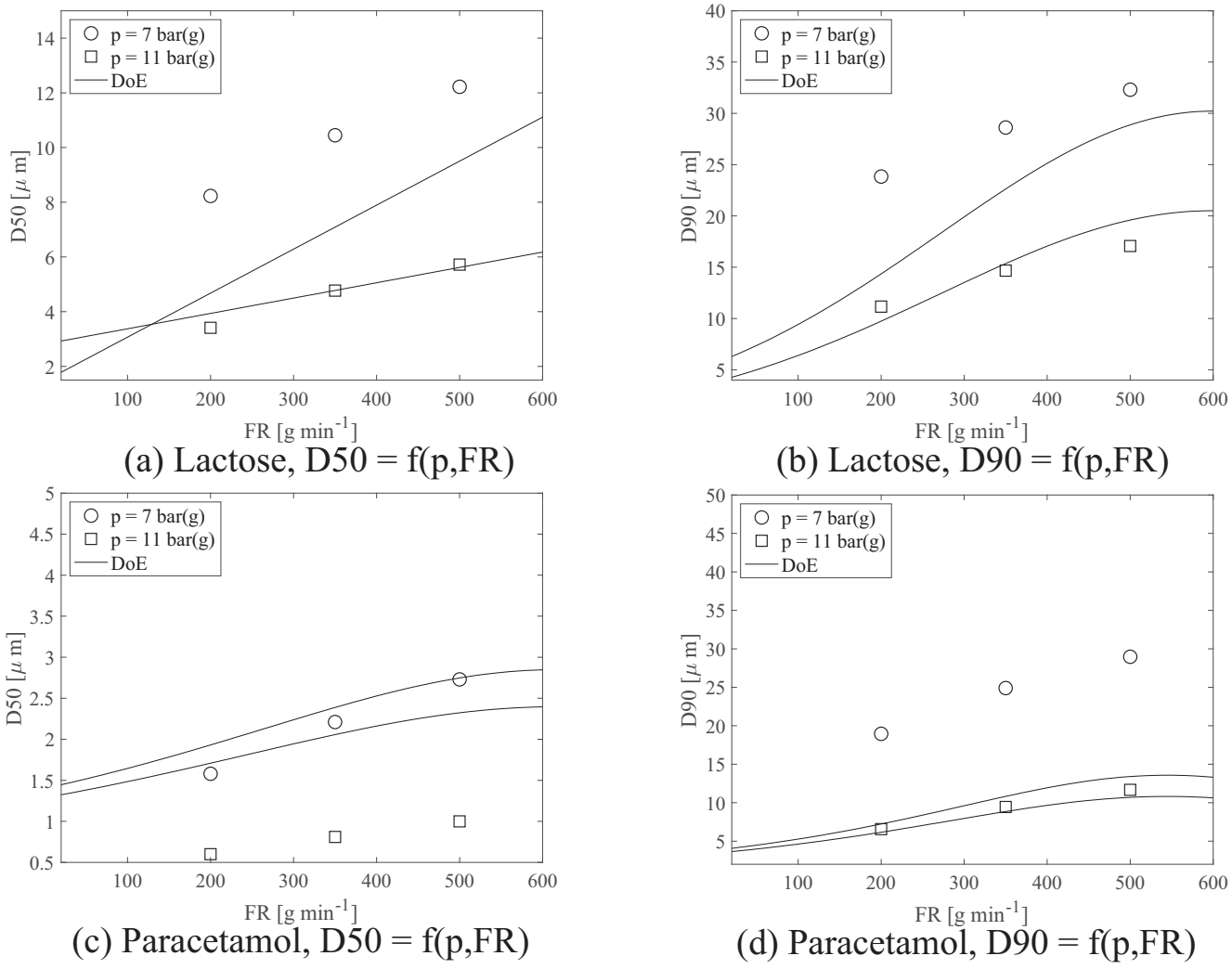

Fig. 13. Predicted/model (markers) and experimental/DOE (lines) results comparison for lactose and paracetamol at 7 and 11 bar(g) at solid feed rates ranging between 20 and 600 g min^{-1}.

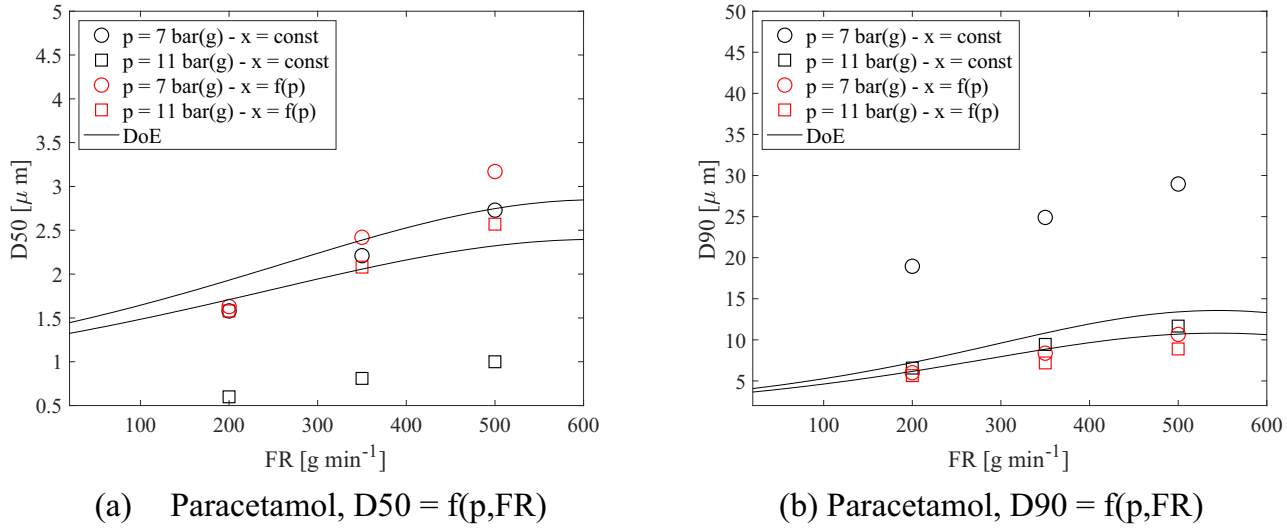

Fig. 14. Averaged-pressure predicted/model (black markers), pressure-dependent predicted/model (red markers) and experimental/DOE (lines) results comparison for paracetamol at 7 and 11 bar(g) at solid feed rates ranging between 20 and 600 g min^{-1}. x represents the vector containing the breakage kernel parameters depicted by Fig. 9. (For interpretation of the references to colour in this figure legend, the reader is referred to the web version of this article.)

account for selectivity dependency on pressure.

Another kernel formulation able to better describe this phenomenon, along with a tribocharging model for the description of the particle electrification due to particle-particle collisions, will be part of a future communication.

Declaration of Competing Interest

The authors declare that there are no competing interest in writing this research paper.

Acknowledgements

This works has been carried out in the framework of the Innosuisse research project (MACH – 37766.1 IP-ENG) developed in collaboration with Jetpharma SA – Switzerland. The Innosuisse funding is gratefully acknowledged.

Appendix A. Appendix

A.1. Linearity and measure consistency control of the micronization dosing unit

Table A.1
Linearity relation intercurring between powder feeder rotation speed – RPM – and the solid feed-rate – FR. $R^2 = 0.9998$.

Feeder speed [RPM]	Feed-rate [g min^{-1}]
0	0
21	22
80	100
165	200
410	500
640	800

Table A.2
Solid feed-rate provided by the dosing unit for $FR_{nom} = 310$ g min^{-1} as function of F and t, with t0 = 0 min, t1 = 2.5 min and t2 = 5 min. F is the percentage of solid loaded into the hopper where F = 100% corresponds to $m_{s,max} = 25$ kg.

F [%]	FR @ t0 [g min^{-1}]	FR @ t1 [g min^{-1}]	FR @ t2 [g min^{-1}]
10	308	306	310
20	312	316	314
50	310	308	310
80	312	300	322

References

[1] C. Sabia, G. Frigerio, T. Casalini, L. Cornolti, L. Martinoli, A. Buffo, D.L. Marchisio, M.C. Barbato, A detailed CFD analysis of flow patterns and single-phase velocity variations in spiral jet mills affected by caking phenomena, Chem. Eng. Res. Des. 174 (2021) 234–253.
[2] S. Bnà, R. Ponzini, M. Cestari, C. Cavazzoni, C. Cottini, A. Benassi, Investigation of particle dynamics and classification mechanism in a spiral jet mill through computational fluid dynamics and discrete element method, Powder Technol. 364 (2020) 746–773.
[3] T. Han, H. Kalman, A. Levy, DEM simulation of particle comminutionin jet milling, Part. Sci. Technol. 20 (2002) 325–340.
[4] M. Ghadiri, Z. Zhang, Impact attrition of particulate solids. Part 1: a theoretical model of chipping, Chem. Eng. Sci. 57 (2002) 3659–3669.
[5] Z. Zhang, M. Ghadiri, Impact attrition of particulate solids. Part 2: experimental work, Chem. Eng. Sci. 57 (2002) 3671–3686.
[6] D.G. Papadopulos, C.S. Teo, M. Ghadiri, T.A. Bell, Attrition of common salt, in: World Congress on Particle Technology, Institution of Chemical Engineers, Worwickshite, U.K, 1998, p. 3.
[7] L. Scott, A. Borissova, A. Burns, M. Ghadiri, Influence of holdup on gas and particle low patterns in a spiral jet mill, Powder Technol. 377 (2021) 233–243.
[8] L. Scott, A. Borissova, A. Burns, M. Ghadiri, Effect of grinding nozzles pressure on particle and fluid flow patterns in a spiral jet mill, Powder Technol. 394 (2021) 439–447.
[9] L. Scott, A. Borissova, A. Burns, M. Ghadiri, Analysis of hold-up and grinding pressure in a spiral jet mill using CFD-DEM, in: EPJ Web of Conferences 249, 2021, p. 12004. Powders and Grains 2021.
[10] S. Bhonsale, L. Scott, M. Ghadiri, J. Van Impe, Numerical simulation of particle dynamics in a spiral jet mill via coupled CFD-DEM, Pharmaceutics 13 (937) (2021) 1–14.
[11] V.M. Masterson, X. Cao, Evaluating particle hardness of pharmaceutical solids using AFM nanoindentation, Int. J. Pharm. 362 (1-2) (2008) 163–171.
[12] M. Meier, E. John, D. Wieckusen, W. Wirth, W. Peuckert, Influence of mechanical properties on impact fracture: prediction of the milling behavior of pharmaceutical powders by nanoindentation, Powder Technol. 188 (3) (2009) 301–313.
[13] S. Zügner, K. Marquardt, I. Zimmermann, Influence of nanomechanical crystal properties on the comminution process of particulate solids in spiral jet mills, Eur. J. Pharm. Biopharm. 62 (2) (2006) 194–201.
[14] O.M. de Vegt, Jet Milling from a Particle Perspective, University of Groningen, 2007. PhD thesis.
[15] D. Wilson, R. Roberts, J. Blyth, Powder Compaction: Process Design and Understanding, from Chemical Engineering in the Pharmaceutical Industry: Drug Product Design, Development, and Modeling. Ch. 9, Second edition, 2019.
[16] X. Cao, M. Morganti, B.C. Hancock, V.M. Masterson, Correlating particles hardness with powder compaction performance, J. Pharm. Sci. 99 (10) (2010) 4307–4316.
[17] L.J. Taylor, D.G. Papadopoulos, P.J. Dunn, A.C. Bentham, J.C. Mitchell, M. J. Snowden, Mechanical characterisation of powders using nanoindentation, Powder Technol. 143 (2004) 179–185.
[18] L. Eriksson, E. Johansson, N. Kettaneh-Wold, C. Wikström, S. Wold, Design of Experiments. Principles and Applications, Learn Ways AB, Stockholm, 2000.
[19] G.K. Batchelor, An Introduction to Fluid Dynamics, Cambridge Univ., 2000. Online ISBN: 9780511800955.
[20] T.H. Shih, W.W. Liou, A. Shabbir, Z. Yang, J. Zhou, A New k-ε Eddy Viscosity Model for High Reynolds Number Turbulent Flows-Model Development and Validation, NASA Technical Memorandum 106721, ICOMP-94–21; CMOTr-94-6, 1994.

[21] H.K. Versteeg, W. Malalasekera, An Introduction to Computational Fluid Dynamics. The Finite Volume Method, Second ed., Pearsons – Prentice Hall, 2007. ISBN: 978-0-13-127498-3.
[22] B.A. Kader, Temperature and concentrations profiles in fully turbulent boundary layers, Int. J. Heat Mass Transf. 24-9 (1981) 1541–1544.
[23] ANSYS Fluent – ANSYS, Inc. https://www.ansys.com/products/fluids/ansys-fluent (accessed October, 2021).
[24] ANSYS, Inc, ANSYS Fluent User's Guide, Release 18.2, 2017.
[25] T. Barth, D. Jespersen, The design and application of upwind schemes on unstructured meshes, in: 27th Aerospace Sciences Meeting, 1989, p. 366.
[26] C.M. Rhie, W.L. Chow, Numerical study of the turbulent flow past an airfoil with trailing edge separation, AIAA J. 21-11 (1983) 1525–1532.
[27] C.T. Kelley, D.E. Keyes, Convergence analysis of pseudo-transient continuation, SIAM J. Num. Anal. 35-2 (1998) 508–523.
[28] H. Konno, S. Saito, Pneumatic conveying of solids through straight pipes, 33rd annual meeting of, J. Chem. Eng. Jpn. 1968 (2-2) (1969) 211–217.
[29] V. Rodniaski, A. Levy, H. Kalman, A new method for simulation of comminution process in jet mills, Powder Technol. 343 (2019) 867–879.
[30] Z. Naumann, L. Schiller, A drag coefficient correlation, Z, Ver. Deutsch. Ing. 77 (318) (1935), e323.
[31] MATLAB, Version 9.9.01538559 (R2020b), The MathWorks, Inc., Natick, Massachusetts, 2020.
[32] A.D. Salman, G.K. Reynolds, J.S. Fu, Y.S. Cheong, C.A. Biggs, M.J. Adams, D. A. Gorham, J. Lukenics, M.J. Hounslow, Descriptive classification of the impact failure model of spherical particles, Powder Technol. 144 (2004) 19–30.
[33] R.C. Rowe, R.J. Roberts, The mechanical properties of powders, Adv. Pharmacol. Sci. 7 (I-IV) (1995) 1–62.
[34] M.H. Shariare, N. Blagden, M. De Matas, F.J.J. Leusen, P. York, Influence of solvent on the morphology and subsequent comminution of ibuprofen crystals by air jet milling, J. Pharm. Sci. 101-3 (2012) 1108–1119.
[35] L.G. Austin, Introduction to the mathematical description of grinding as rate process, Powder Technol. 5 (1971).
[36] H.J.C. Gommeren, D.A. Heitzmann, H.J.M. Kramer, K. Heiskanen, B. Scarlett, Dynamic modelling of a closed loop jet mill, Int. J. Miner. 44-45 (1996) 407–506.
[37] H.J.C. Gommeren, D.A. Heitzmann, J.A.C. Moolenaar, B. Scarlett, Modelling and control of a jet mill plant, Powder Technol. 108 (2000) 147–154.
[38] S. Kukkonen, J. Lampinen, GDE3: The third evolution step of generalized differential evolution, IEEE Congr. Evol. Comput. 1 (2005) (2005) 443–450.
[39] D. Baur, Design, Modeling and Optimization of Multi-Column Chromatographic Processes, Doctoral dissertation, ETHZ, 2017.